

Effect of size on the magnetic properties and crystal structure of magnetically frustrated DyMn₂O₅ nanoparticles

T. Tajiri,^{1,*} H. Deguchi,² M. Mito,² K. Konishi,³ S. Miyahara,¹ and A. Kohno¹

¹*Faculty of Science, Fukuoka University, Fukuoka 814-0180, Japan*

²*Graduate School of Engineering, Kyushu Institute of Technology, Kitakyushu 804-8550, Japan*

³*Graduate School of Science and Engineering, Ehime University, Matsuyama 790-8577, Japan*



(Received 7 June 2018; published 9 August 2018)

We synthesized magnetically frustrated DyMn₂O₅ nanoparticles in pores of mesoporous silica, with particle sizes ranging from 7 to 20 nm, and investigated their magnetostructural correlation. We found that the lattice constants of the DyMn₂O₅ nanoparticles deviated from those of the bulk crystal below ~ 12 nm and their crystallographic structures at the unit cell level were distorted. The size dependences of the blocking temperature and coercive field drastically change at ~ 12 nm. In addition, the Weiss temperature depends strongly on particle size, and its sign changes at ~ 12 nm. It is considered that such features can be realized owing to the distortion caused by the ligand atoms at the surface. The orbital structures of the magnetic sites are easily modified due to the distortion of the ligand ions at the surface, so that the correlation between the crystal structure and magnetic properties can be enhanced. Moreover, magnetization of the nanoparticle results in quasi-superparamagnetic behavior. Monte Carlo calculation of the nanoparticles indicates that such a feature is realized due to the quasi-free spins induced at the surface by magnetic frustration.

DOI: [10.1103/PhysRevB.98.064409](https://doi.org/10.1103/PhysRevB.98.064409)

I. INTRODUCTION

Nanoparticles, because of their large fraction of surface atoms and finite size effects, possess interesting magnetic properties and crystal structures, which differ from those of the bulk crystals. Although most of the features of the nanoparticles can be explained using the magnetic phase diagram and electronic state of the bulk crystal, finite size effects can induce novel features that are not expected in the bulk crystal. Recently, nanoparticles of strongly correlated materials have been attracting attention [1]. They show anomalous size effects due to a complex phase diagram realized by the competition between the strong couplings induced by the lattice, spin, charge, and orbital degrees of freedom. One of the typical examples of strongly correlated materials is Mn-oxide. Mn-oxides show unusual characteristics such as colossal magnetoresistance and magnetoelectric multiferroic behaviors in the bulk crystal [2,3] and nanoparticles of Mn-oxides are expected to possess novel features. In fact, we have already shown that the nanoparticles of the multiferroics, (La, Sr)MnO₃ [4,5], DyMnO₃ [6], and BiMnO₃ [7], exhibit characteristic size dependences on their magnetic properties and crystallographic structures, which are different from those of conventional nanoparticles. Moreover, the nanoparticles of these materials reveal a variety of size dependences reflecting the various characters of the bulk crystal. Such anomalous effects are the result of the strong correlations between the magnetic properties and crystal structures.

Rare earth manganese oxides RMn₂O₅ (R = rare earth elements Dy, Tb, Y, and Bi) are known as multiferroic materials

and exhibit strong correlations between the magnetic and dielectric properties and crystallographic structures [8–16]. RMn₂O₅ exhibits magnetoelectric effects and spontaneous electrical polarization just below the antiferromagnetic ordering temperature. Bulk RMn₂O₅ consists of linked Mn⁴⁺O₆ octahedra and Mn³⁺O₅ pyramids. Figure 1(a) shows the crystal structure of DyMn₂O₅, which has orthorhombic crystallographic symmetry with the space group *Pbam*, in which the Mn⁴⁺O₆ octahedra share edges to form ribbons parallel to the c axis and adjacent ribbons are linked by pairs of corner-sharing Mn³⁺O₅ pyramids [12,15,17]. It undergoes an antiferromagnetic transition for the spin of the Mn sublattice at ~ 40 K, which is characterized by the existence of the commensurate-incommensurate transition of the Mn spin structure at a lower temperature. The antiferromagnetic ordering of the R ions occurs at $T_N(R) \sim 10$ K. Their lattice geometry causes an inherent magnetic frustration, which is lifted by a small shift of the Mn³⁺ cations, resulting in a canted antiferroelectric phase that is strongly coupled to the magnetic structure. The magnetic interaction in RMn₂O₅ is considered to be Ising type, whereas that for RMnO₃ is cycloidal type [18–21]. In addition, the crystal structure of the two compound system is disparate. Therefore, it is expected that RMn₂O₅ nanoparticles exhibit the size effects on their magnetic properties and crystal structure that are different from those of the RMnO₃ nanoparticles. In this study, we investigated the crystal structure and magnetic properties of DyMn₂O₅ nanoparticles. In DyMn₂O₅, Mn ions exhibit an antiferromagnetic order below $T_N(\text{Mn}) \sim 42$ K and incommensurate-commensurate transition at $T_N \sim 30$ K, and the Dy spin order modifies the Mn spin structures below $T_N(\text{Dy}) \sim 8$ K [15,22–26]. Below $T_N(\text{Mn})$, the neighboring Mn³⁺ spins are antiferromagnetically ordered, while the Mn⁴⁺ spins exhibit spiral ordering along the c axis. The spins of

*tajiri@fukuoka-u.ac.jp

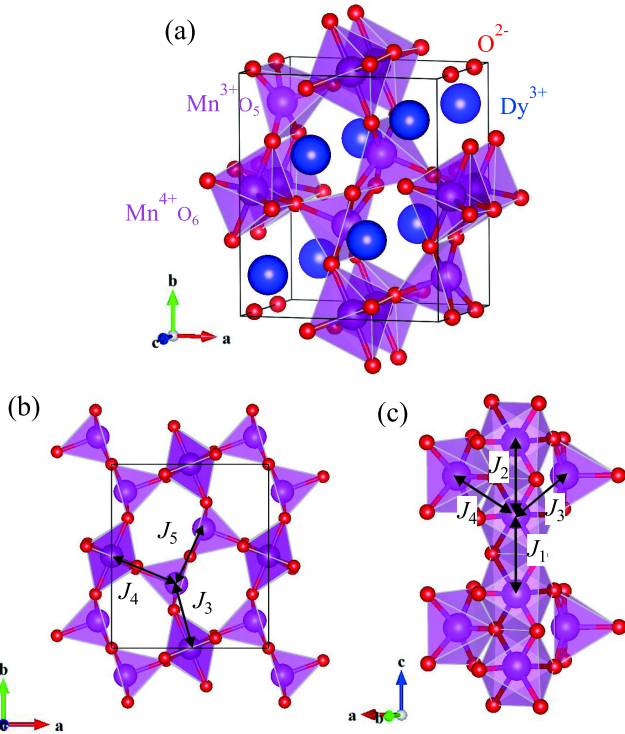


FIG. 1. (a) Crystal structure of DyMn_2O_5 showing distorted Mn^{4+}O_6 ($S=3/2$) octahedra cross linked with distorted Mn^{3+}O_5 ($S=2$) square pyramids. The five nearest-neighbor magnetic interactions between the spins of the Mn ions in the ab plane (b) and along c axis (c) are also illustrated.

DyMn_2O_5 lie in the ab plane. Within the ab plane, DyMn_2O_5 has two zigzag chains per unit cell and the antiferromagnetically coupled nearest neighbors Mn^{4+} and Mn^{3+} are aligned in a direction parallel to the a axis. The lattice geometry gives rise to competition among the five nearest-neighbor magnetic interactions involving the spins of the Mn ions [9,15,24,27,28] as shown in Figs. 1(b) and 1(c), which induces frustrations of the magnetic couplings. The several phase transitions observed at low temperatures may be induced by the highly frustrated magnetic couplings.

Recently, we reported the anomalous magnetic properties and crystal structure of the DyMn_2O_5 nanoparticles of size ~ 7 nm. The magnetic properties, crystal structures, and lattice constants are different from those of the bulk crystal [29]. To clarify the origin of the anomalous properties of the DyMn_2O_5 nanoparticle, we attempt to establish the particle size dependence of the magnetic properties and crystal structures in this study. We synthesized DyMn_2O_5 nanoparticles of several particle sizes, ranging from 7 to 20 nm, and elucidated the particle size dependence using powder x-ray diffraction (XRD), magnetization, and dc and ac magnetic susceptibilities. The experimental results indicate that pronounced changes in both the crystal structure and magnetic properties occur at a particle size of ~ 12 nm, as described in the following sections. In addition, theoretical investigations of the nanoparticles by the Monte Carlo method indicated that the observed anomalous behavior is associated with the inherent magnetic frustration of DyMn_2O_5 .

II. EXPERIMENTAL

DyMn_2O_5 nanoparticles were synthesized in the one-dimensional pores (with a diameter of ~ 7 nm) of the mesoporous silica SBA-15. SBA-15 was used as a template to equalize particle size during the fabrication of the DyMn_2O_5 nanoparticles and deflocculate the synthesized nanoparticles because it has a well-ordered two-dimensional hexagonal mesoporous structure and its one-dimensional pores are separated by silica walls [30]. The DyMn_2O_5 nanoparticles were synthesized by soaking SBA-15 in a stoichiometric aqueous solution of $\text{Dy}(\text{CH}_3\text{COO})_3 \cdot 4\text{H}_2\text{O}$ and $\text{Mn}(\text{CH}_3\text{COO})_2 \cdot 4\text{H}_2\text{O}$. The soaked samples were then dried and calcinated in an oxygen atmosphere [29].

Transmission electron microscopy (TEM) images of the DyMn_2O_5 nanoparticles synthesized in SBA-15 were obtained by using a JEOL JEM-2100 Transmission Electron Microscope operating at 200 kV. The powder XRD measurements for the nanoparticles were carried out at room temperature by using a synchrotron radiation x-ray diffractometer with a Debye-Scherrer camera at the beamline BL-8B at the Photon Factory of the Institute of Materials Structure Science, High Energy Accelerator Research Organization (KEK), and at the beamline BL02B2 of SPring-8. We used incident x rays of energy 18 keV and their wavelength was calibrated using the XRD pattern of CeO_2 powder. The magnetic properties of the nanoparticles were investigated by using a superconducting quantum interference device (SQUID) magnetometer (Quantum Design, Inc.). The dc magnetic susceptibilities were measured under an external magnetic field of 100 Oe in both field-cooling (FC) and zero-field-cooling (ZFC) conditions. The ac susceptibility was measured in an ac magnetic field with frequency ranging from 0.3 to 1000 Hz and amplitude 3.8 Oe. Magnetization curves were obtained up to 5 T at 5 and 15 K.

III. RESULTS OF EXPERIMENTS AND MONTE CARLO CALCULATIONS

A. Structural analysis

We observed the powder XRD patterns of the DyMn_2O_5 nanoparticles synthesized in the pores of SBA-15. Figure 2 shows the powder XRD patterns for three representative nanoparticles, for which the mean particle sizes d were estimated to be 7.2, 11.1, and 14.7 nm. The diffraction patterns of all the DyMn_2O_5 nanoparticles exhibited broad Bragg peaks, which were attributed to the orthorhombic symmetry with space group $Pbam$ [12,17], and also contained the impurity compound Dy_2O_3 , which is indicated by an asterisk in Fig. 2. The observed broad diffraction peaks were deconvoluted to those associated with DyMn_2O_5 by multipeak fitting. Note that the particle sizes of all the DyMn_2O_5 nanoparticles were estimated based on the peak positions and the full widths at half maximum of the Bragg peaks, using Scherrers equation. The validity of the particle-size estimation was confirmed through TEM. Figure 3 shows a TEM image of representative DyMn_2O_5 nanoparticles, with a mean particle size of $d = 8.5$ nm estimated from an XRD analysis in the pores of SBA-15. The linearly aligned dark spots in the TEM image correspond to the DyMn_2O_5 nanoparticles dispersed in the

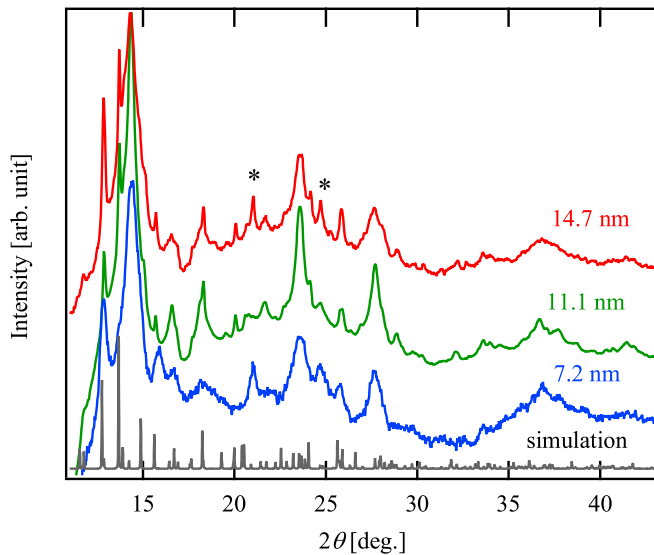


FIG. 2. Powder XRD patterns for three DyMn_2O_5 nanoparticles of particle sizes 7.2, 11.1, and 14.7 nm in SBA-15 and the simulated pattern for the bulk crystal. The wavelength of the incident x rays was 0.688 Å. The asterisks indicate the impurity phase Dy_2O_3 .

pores of SBA-15. The inset of Fig. 3 shows the histogram of the particle-size distribution obtained from the TEM image. The histogram was fitted by a log-normal function [31] with a peak position of $d_0 = 7.80$ and width 0.18, as shown in the inset of Fig. 3; this results in a mean particle size d of 7.39 nm and standard distribution $\sigma = 1.03$ nm. The histogram indicates a narrow size distribution [31]. Thus, the mean particle size estimated from the TEM image is consistent with that obtained from XRD. Thus, the XRD measurement results indicated the successful synthesis of the DyMn_2O_5 nanoparticles with sizes

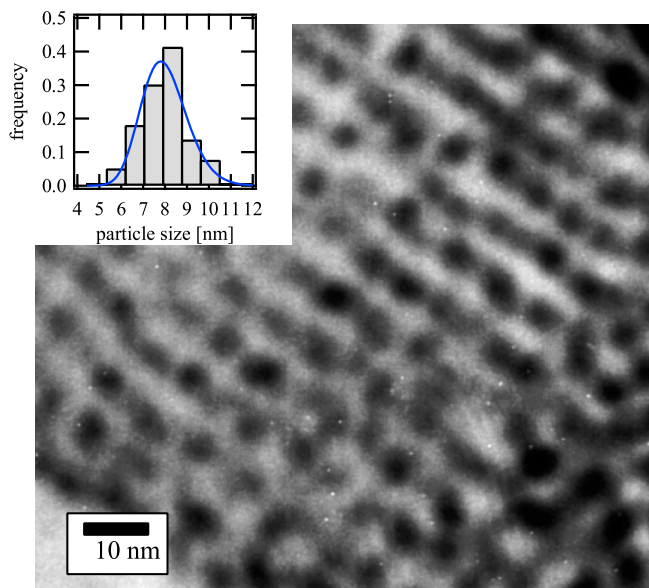


FIG. 3. TEM image of DyMn_2O_5 nanoparticles synthesized in the pores of SBA-15 with a mean particle size of 8.5 nm. The inset shows a histogram of the particle-size distribution. The solid line represents the fitting curve based on a log-normal function.

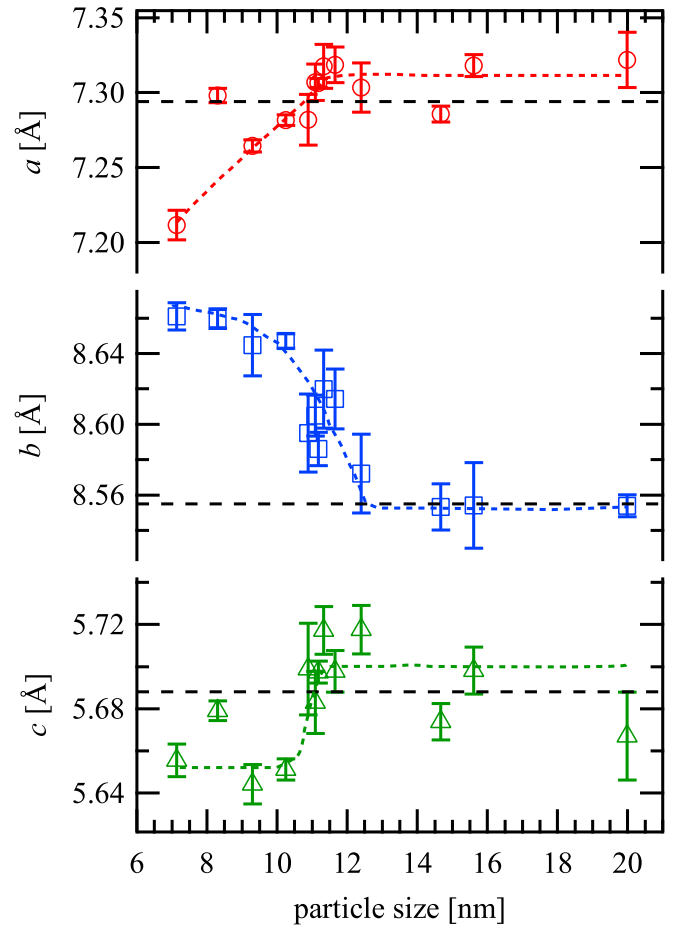


FIG. 4. Particle-size dependence of the lattice constants of DyMn_2O_5 nanoparticles. The horizontal dashed lines show the lattice constants of the bulk crystal.

ranging from 7 to 20 nm. Hereafter, we use the values estimated from XRD to describe the particle sizes.

The lattice constants of the DyMn_2O_5 nanoparticles were estimated from the XRD patterns. The lattice constants were calculated from the relation between the lattice constants and the plane indices determined from the Bragg peak angles for all the deconvoluted peaks. Figure 4 shows the particle size dependences of the lattice constants a , b , and c of the DyMn_2O_5 nanoparticles. The estimated lattice constants of the nanoparticles with $d > 12$ nm are almost constant, and are consistent with those of the bulk crystals, as shown by the dotted horizontal lines in Fig. 4. On the other hand, the lattice constants of the nanoparticles with $d < 12$ nm are modulated from those of the bulk crystals. As the particle size decreases, the lattice constants a and c decrease, whereas the lattice constant b increases monotonically. These results suggest that the crystallographic structure of the DyMn_2O_5 nanoparticles is distorted anisotropically compared to that of the bulk crystal.

B. Magnetic measurements

We measured the dc and ac susceptibilities and magnetization curve of the DyMn_2O_5 nanoparticles. As a typical example, the temperature dependences of the dc magnetic susceptibilities of the nanoparticle with $d = 10.4$ nm in both

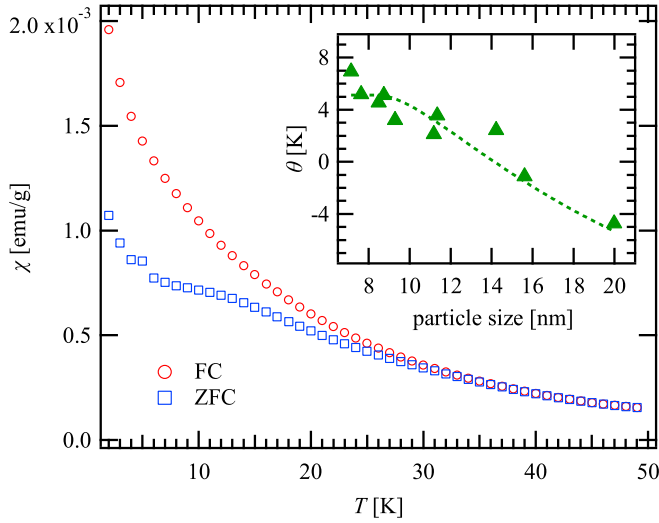


FIG. 5. Temperature dependence of the dc magnetic susceptibilities of DyMn_2O_5 nanoparticles of particle size 10.4 nm under an external magnetic field of 100 Oe in the field-cooled (red circle symbols) and zero-field-cooled (blue square symbols) conditions. The inset shows the particle-size dependence of the Weiss temperature estimated by Curie-Weiss fitting. The dashed line is the fitting result (please refer to the text).

the FC and ZFC conditions are shown in Fig. 5. Both the FC and ZFC susceptibilities increase as the temperature decreases. The rapid increase in both the susceptibilities below 10 K is attributed to the magnetic ordering of the Dy spins. A pronounced magnetic irreversibility between the FC and ZFC susceptibilities was observed below ~ 30 K (T_{irr}). The ZFC susceptibility exhibits a hump at ~ 15 K, which corresponds to the blocking temperature T_B , corresponding to the blocking phenomena of superparamagnetism. The dc susceptibilities of the DyMn_2O_5 nanoparticles with $d = 7\text{--}20$ nm show qualitatively the same behaviors. Note that, as particle size increases, the T_{irr} increases from 41 K for 7.2 nm to 70 K for 20 nm. In the case of RMnO_3 bulk crystals, which show magnetoelectric effect and paramagnetic-incommensurate antiferromagnetic transition of the Mn spin that is the same as DyMn_2O_5 , a pronounced magnetic irreversibility exists between the FC and ZFC susceptibilities below the incommensurate antiferromagnetic transition temperature $T_N(\text{Mn})$ [32]. It suggests that the observed T_{irr} for the DyMn_2O_5 nanoparticles corresponds to $T_N(\text{Mn})$.

In the high-temperature region $150 \text{ K} \leq T \leq 300 \text{ K}$, the temperature dependence of the dc susceptibility fits well with the Curie-Weiss law. Thus, we can evaluate the Weiss temperature from the fitting. The particle size dependence of the Weiss temperature θ is shown in the inset of Fig. 5. As the particle size decreases, the sign of the Weiss temperature changes from negative to positive at ~ 12 nm. Note that the Weiss temperature of the DyMn_2O_5 bulk crystals is estimated to be negative, -26 K. In Mn oxides, the effective magnetic interaction correlated with the Weiss temperature strongly depends on the orbital structures of the Mn ions [20,33–35]. Since the modulation of the orbital can be enhanced around the surface due to a lack of ligand atoms and/or the modulation of the ligand atom positions, we assume that the modulation

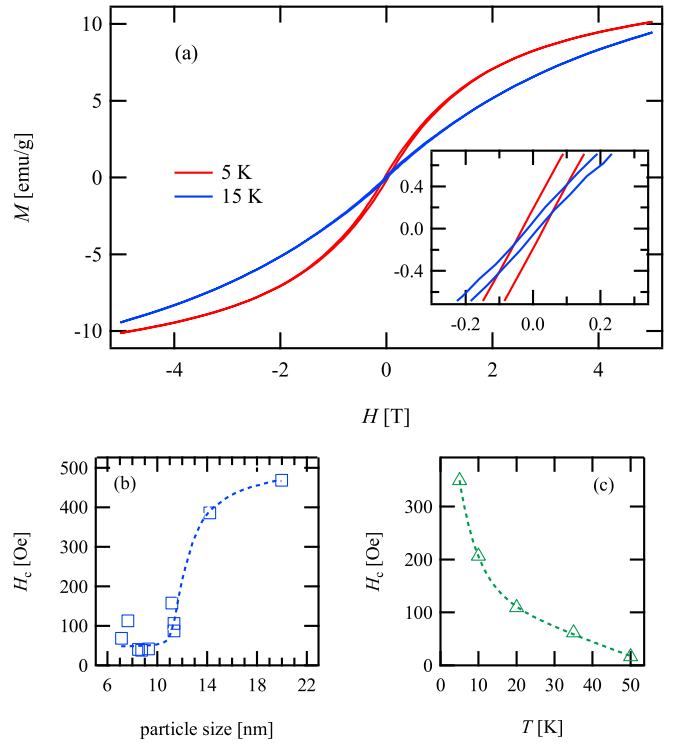


FIG. 6. (a) Magnetization curves for DyMn_2O_5 nanoparticles of particle size 11.1 nm at 5 and 15 K. The inset shows a magnification of the low field region of the hysteresis loop. (b) Particle-size dependence of the coercive field at 15 K. (c) Temperature dependence of the coercive field for nanoparticles with $d = 11.1$ nm.

of the interactions mainly occurs around the surface of the nanoparticles. As a simple model, we introduce a cylinder-shaped particle of radius r and height h , and define that the region $r > r_s$ is a shell region of the nanoparticle. The obtained Weiss temperature should be derived from both the magnetic moment at the surface and that in the core of the nanoparticles. For simplicity, we assume that the Weiss temperature in the core θ_c is identical to that in the bulk crystal, $\theta_c = -26$ K, whereas the Weiss temperature in the shell θ_s is a fitting parameter. In addition, we assume that the depth of the shell region r_s does not depend on the particle size and is determined from the fit. Here, the Weiss temperature of a nanoparticle is defined as

$$\theta = \theta_s \left[1 - \frac{(r - r_s)^2}{r^2} \right] + \theta_c \frac{(r - r_s)^2}{r^2}, \quad (1)$$

where $r = d/2$. From the fit of the data, shown in the inset of Fig. 5, the values $\theta_s = 5.1$ K and $r_s = 4.2$ nm are obtained. The results indicate that ferromagnetic interaction is dominant in the shell. When $d \leq 10$ nm, the number of core spins is negligible. Thus, the magnetic properties of the nanoparticle with $d \leq 10$ nm are a result of the modulated magnetic interactions with ferromagnetic Weiss temperature, and can be strongly modified from those of the bulk crystals, which is consistently with the experimental observations.

Figure 6(a) shows the magnetization curves for the DyMn_2O_5 nanoparticles with $d = 11.1$ nm at 5 and 15 K. The curves exhibit a hysteresis loop below

$T_{\text{irr}} = 43$ K. Both the coercive field H_c and the magnitude of magnetization are larger at the lower temperature. Figure 6(b) shows the size dependence of the coercive field H_c for the DyMn_2O_5 nanoparticles at 15 K. For particles smaller than ~ 12 nm, H_c remains almost constant, and drastically increases at around 12 nm. For particles larger than 12 nm, H_c gradually increases with increasing particle size. Figure 6(c) shows the temperature dependence of H_c for the particle with $d = 11.1$ nm. H_c increases with decreasing temperature below T_{irr} . This behavior is derived from the ordered spins with ferromagnetic correlations at the surface of the nanoparticles. Another unusual feature of the magnetization of the DyMn_2O_5 nanoparticles is the quasiparamagnetic behavior observed even below T_{irr} . Since the spontaneous magnetization and hysteresis are quite small [Fig. 6(a)], the magnetization above H_c shows the quasiparamagnetic behavior. By fitting the magnetization curve to a Langevin function, we determined that the magnetic moment is about $14\mu_B$. This value of the magnetic moment is independent of the particle size. We also note that the magnetization curves for the nanoparticles are different from that of the DyMn_2O_5 bulk crystal, which does not exhibit the hysteresis loop and increased linearly with magnetic field at 10 K, and the magnetization of the DyMn_2O_5 bulk crystal linearly increases for low fields, showing a kink at 1.52 T [14], before slowly saturating for the a or b direction for H above 3 T, indicating the presence of a H -induced phase transition at 1.52 T at 3 K [23,26]. We considered that such observed behavior is a unique feature of magnetically frustrated nanoparticles with both ferromagnetic and antiferromagnetic interactions. Because of the magnetic frustration, the mean-field interactions of the spins at the surface can be suppressed, which results in quasi-free spins at the surface. Thus, the magnetization around the surface behaves as a quasi-free spin and dominates for small magnetic fields. Moreover, the ferromagnetic interactions around the edge brought about a cluster of spins. The moment $14\mu_B$ may correspond to the spin cluster, which consists of Mn^{4+} ($2\mu_B$), Mn^{3+} ($3/2\mu_B$), and Dy sites. Thus, the magnitude of the spontaneous magnetization and H_c may be effectively determined by the local conditions around the surface, i.e., the lattice distortion, which is qualitatively consistent with the particle size dependence [Fig. 6(b)]. An exchange bias is often observed in the core-shell model nanoparticles with ferromagnetic and antiferromagnetic phases. In this study, the DyMn_2O_5 nanoparticles did not exhibit an exchange bias, which suggests that the strong uniaxial anisotropy does not occur between the quasi-free spins at the surface and the magnetically frustrated spins in the core of the DyMn_2O_5 nanoparticles.

Figure 7(a) shows the ac magnetic susceptibilities of the DyMn_2O_5 nanoparticles of particles size 11.3 nm for frequencies ranging from 0.3 to 300 Hz and amplitude 3.8 Oe of the ac magnetic field. Both the in-phase (χ') and out-of-phase χ'' susceptibilities of all the nanoparticles increase below ~ 40 K and exhibit a peak due to the blocking phenomena at ~ 15 K. Both the peaks of $\chi'(T)$ and $\chi''(T)$ shift toward higher temperatures with increasing frequency. The observed relaxation behavior was a consequence of the superparamagnetic behavior. Figure 7(b) shows the size dependence of the blocking temperature T_B for the DyMn_2O_5 nanoparticles at 100 Hz. As the particle size decreases, the blocking temperature decreases

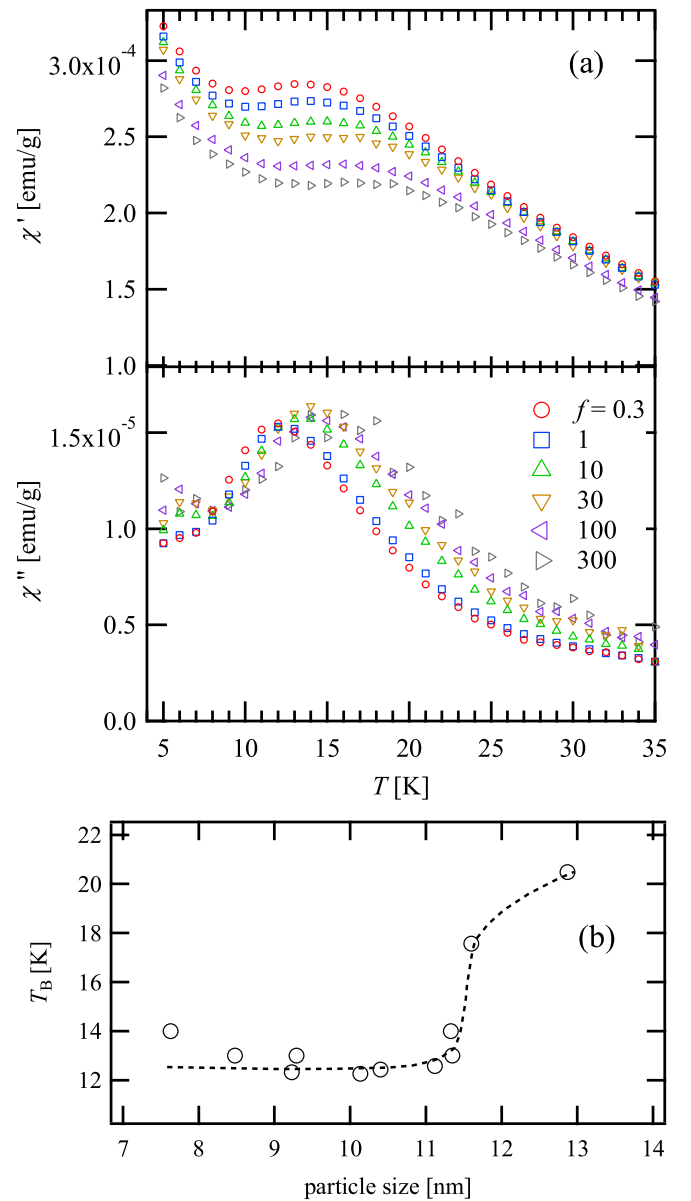


FIG. 7. (a) Temperature dependence of in-phase (upper panel) and out-of-phase (lower panel) susceptibilities for DyMn_2O_5 nanoparticles of particle size 11.3 nm in the frequency range 0.3–300 Hz in a zero dc field. (b) Particle-size dependence of the blocking temperature at 100 Hz.

monotonically until the size reaches ~ 11 nm and remains almost constant below ~ 11 nm. The size dependence of T_B is qualitatively consistent with that of H_c . The observed relaxation behavior for the DyMn_2O_5 nanoparticles is evaluated based on Néel-Brown relaxation. Here, we estimated the effective relaxation time τ from the fitting of $\chi''(\omega)$, as shown in the inset of Fig. 8 [36]. Figure 8 shows the particle size dependence of τ for the DyMn_2O_5 nanoparticles. The τ for the DyMn_2O_5 nanoparticles exhibits the characteristic size dependence: as the particle size decreases, τ is almost constant, until the particle size reaches ~ 12 nm, and remarkably increases below ~ 12 nm. The particle size dependences of the coercive field, blocking temperature, and relaxation time exhibit a significant

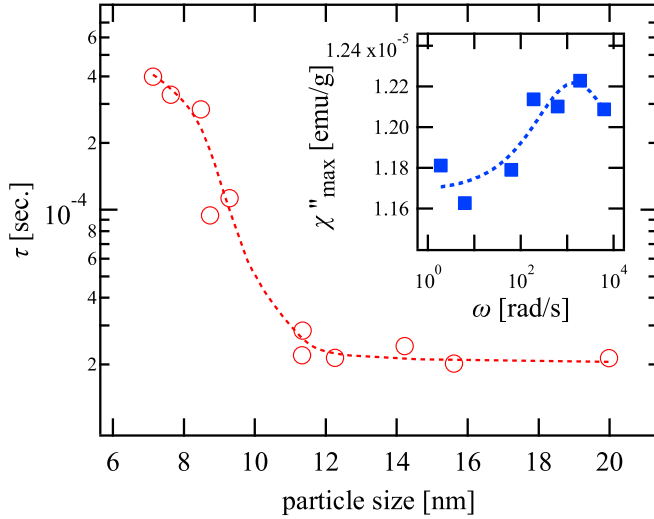


FIG. 8. Particle size dependence of the effective relaxation time. The inset shows the fitting results of $\chi''(\omega)$ for $d = 9.3$ nm. The dashed line in inset is the fitting result.

change at ~ 12 nm, since the features of the quasi-free spins around the surface, which are induced by the frustrations, are dominant for a particle with $d \lesssim 12$ nm. The properties of the quasi-free spins are determined by the local characteristics, i.e., the anisotropic energy barriers for a single spin (or a few-spin cluster), and not by those of the whole particle. As a result, factors such as the blocking temperature and magnetic moment are hardly dependent on the nanoparticle size. Moreover, the anisotropic energy barriers strongly depend on the surface lattice structure, and numerous values of these energies exist. Thus, it is likely that we observe the average of them from T_B and the minimum values from H_c , which may be a reason for the hysteresis in the magnetization curve below T_B .

C. Monte Carlo calculation

To confirm the quasi-free behaviors of the spins around the surface, we performed a Monte Carlo calculation for the nanoparticles with classical spins. The essence of DyMn_2O_5 may be described by the two-dimensional frustrated Heisenberg model [15] (Fig. 9) under the external magnetic field B^{ex} :

$$\begin{aligned}
 H = & -J_3 \sum \mathbf{S}_i \cdot \mathbf{T}_j - J_4 \sum \mathbf{S}_i \cdot \mathbf{T}_j - J_5 \sum \mathbf{T}_i \cdot \mathbf{T}_j \\
 & - g\mu_B \sum \mathbf{B}^{\text{ex}} \cdot \mathbf{S}_i - g\mu_B \sum \mathbf{B}^{\text{ex}} \cdot \mathbf{T}_i \\
 & - K_{xy} \sum (S_i^x \cos \phi_i + S_i^y \sin \phi_i)^2 \\
 & - K_z \sum (S_i^z)^2 - K_z \sum (T_i^z)^2, \quad (2)
 \end{aligned}$$

where $\mathbf{S}_i(\mathbf{T}_i)$ is a spin operator with $S = 2$ ($T = 3/2$) and represents a spin at the Mn^{4+} (Mn^{3+}) site. g is a g -value and μ_B is Bohr magneton. $J_3, J_4,$ and J_5 are the exchange interactions (see Fig. 9). The K_{xy} term is the uniaxial anisotropy of the Mn^{4+} spin. ϕ_i is fixed to be $\pi/3$ at the A-site and $-\pi/3$ at the B-site. The $K_z (< 0)$ term is the hard uniaxial anisotropy, which realizes an in-plane spin structure. For simplicity, we neglect the other anisotropy terms. Here, we assume ferromagnetic interactions for the J_3 bond and antiferromagnetic interactions

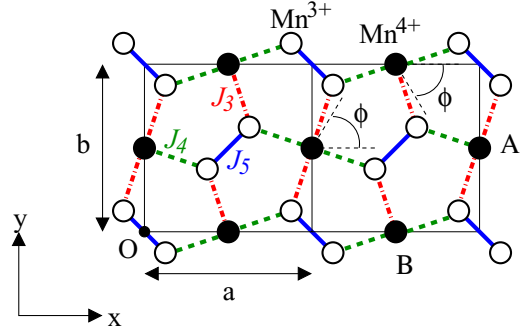


FIG. 9. Heisenberg model with J_3, J_4, J_5 interactions. The open (filled) circles represent Mn^{3+} (Mn^{4+}) sites. The point O is defined as the center of the nanoparticle. The lattice constants a and b are fixed as $a = 7.294$ Å and $b = 8.551$ Å [15]. ϕ_i is fixed to be $\pi/3$ at the A-site and $-\pi/3$ at the B-site.

for the J_4 and J_5 bonds to realize the competition between the ferromagnetic and antiferromagnetic interactions, since the experimental results indicated the sign change of the Weiss temperature with decreasing particle size.

The Monte Carlo calculation has been performed for the nanoparticles with classical spins, given by Eq. (2). The Metropolis single spin-flip algorithm was used and 8000 samples were taken. The nanoparticle was assumed to be a circle with its diameter d in a two-dimensional plane and center fixed at the point O shown in Fig. 10. For simplicity, we neglect the effects of lattice distortion. The lattice constants $a = 7.294$ Å and $b = 8.551$ Å and the positions of the Mn

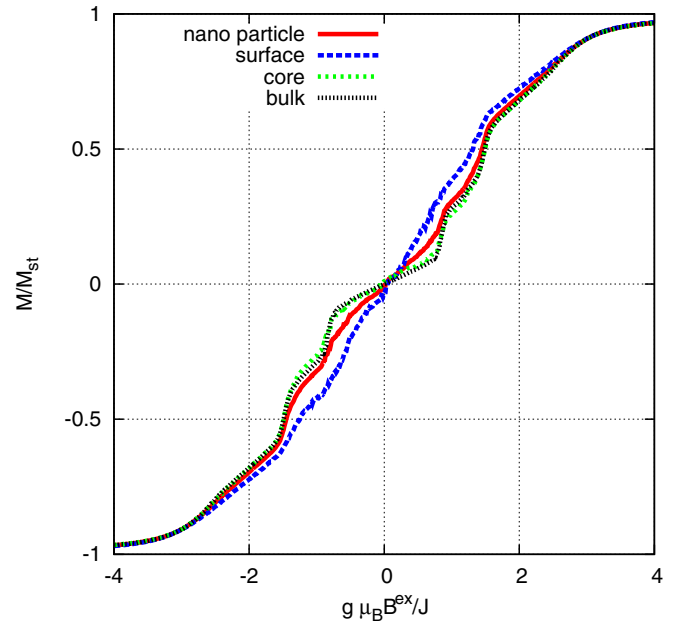


FIG. 10. Magnetization of a nanoparticle with $d = 10$ nm with increasing external magnetic $\mathbf{B}^{\text{ex}} \parallel y$ at $T/J_5 = 0.1$. As a reference, the magnetization of the bulk system is also shown. The calculated results for the surface and core parts correspond to the magnetization owing to only the regions of the surface ($r \geq 4$ nm) and core ($r \leq 4$ nm) parts, respectively, where r is the distance from the center of the nanoparticle.

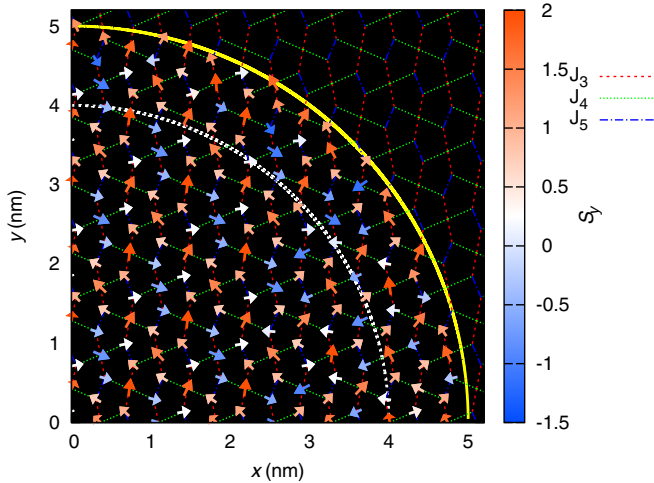


FIG. 11. Spin structure of a nanoparticle with $d = 10$ nm when $g\mu_B \mathbf{B}^{ex}/J_5 = 0.5$ ($\mathbf{B}^{ex} \parallel y$) and $T/J_5 = 0.1$. The center of the nanoparticle is located at $O = (0, 0)$. The results for $x \geq 0$ and $y \geq 0$ are shown. The expectation values of the in-plane components of the spins ($\langle S_i^x \rangle$, $\langle S_i^y \rangle$) are shown by arrows and their color represents the $\langle S_i^y \rangle$ at each site. The nanoparticle (core) region is bounded by the yellow solid (white dashed) line.

sites were taken from Ref. [15]. We performed the calculation for various parameters for $J_3 < |J_4| < |J_5|$, which can stabilize the ground-state spin configuration observed in the bulk material, and found that the qualitative features hardly depend on the interactions unless we restricted ourselves to the case $J_3 < |J_4| < |J_5|$. Thus, we show the results for $J_3/|J_5| = 0.3$, $J_4/|J_5| = -0.4$, $K_{xy}/|J_5| = 0.5$, $K_z/|J_5| = -0.5$, and $J_5 = -1$ as a typical example.

The magnetization of a nanoparticle of diameter $d = 10$ nm with increasing external magnetic field $\mathbf{B}^{ex} \parallel y$ at $T/J_5 = 0.1$ is shown in Fig. 10. As a reference, the results for 12×12 unit cells with a periodic boundary condition, where the system size effects are negligible, are also shown as those corresponding to the bulk. To clarify the origin of the difference between the magnetization in the nanoparticle and that in the bulk, we divide the nanoparticle into the core ($r \leq 4$ nm) and surface ($r \geq 4$ nm) parts, where r is the distance from the center of the nanoparticle, and plot the magnetization of each part (Fig. 10). The magnetization of the core part is almost identical to that of the bulk system. On the other hand, the magnetization at the surface is easily aligned by the external magnetic field and shows quasi-free spin behaviors. As a result, the magnetization at the surface is dominant when $g\mu_B \mathbf{B}^{ex}/J_5 \lesssim 1$. To clarify these points, the in-plane components of the spins ($\langle S_i^x \rangle$) and ($\langle S_i^y \rangle$) at each site when $g\mu_B \mathbf{B}^{ex}/J_5 = 0.5$ are shown in Fig. 11. Figure 11 indicates that the ferromagnetic components are dominant in the surface region ($r \geq 4$ nm). Thus, the magnetization of the magnetically frustrated nanoparticles behaves as a quasi-free spin. Such a feature is qualitatively consistent with the experimental observations. Note that we performed the calculation for $d = 6, 8, 12, 16,$ and 32 nm and confirmed that the qualitative features hardly depend on the particle sizes.

The theoretical study indicates that the DyMn_2O_5 nanoparticles exhibit a magnetization induction due to the reduction in particle size. The induction of magnetization has also

been reported in NiO nanoparticles, which is attributed to multisublattice spin configurations. The calculated spin configuration in the NiO nanoparticles is 8-, 6-, or 4-sublattice spin ordering with decreasing particle size [37,38]. The origin of the induction of magnetization is different between the DyMn_2O_5 and NiO nanoparticles. The present calculations suggest that the observed magnetization induction in the DyMn_2O_5 nanoparticles is characteristic of nanoparticles of magnetically frustrated materials.

IV. DISCUSSION

The crystallographic structure of the DyMn_2O_5 nanoparticles was distorted anisotropically at the unit cell level below ~ 12 nm: the lattice constants a and c decrease while the lattice constant b increases as the particle size decreases, especially the distortion of the ab plane was pronounced. The magnetic measurement results for the DyMn_2O_5 nanoparticles with sizes ranging from 7 to 20 nm reveal characteristic size dependences. The particle size dependences of blocking temperature, coercive field, and relaxation time exhibit the same behavior qualitatively: the tendency of the size dependences changes significantly at ~ 12 nm. The changes in the H_c , T_B , and τ are attributed to the change in the magnetic anisotropy around the surface of the nanoparticle. The magnetization curves exhibit a hysteresis loop below $T_N(\text{Mn})$. In addition, as the particle size increases, the sign of the Weiss temperature changes from positive to negative at ~ 12 nm. The present experimental results indicate a strong correlation between the changes in the magnetic properties and the distortion of the crystallographic structure. Such characteristics can be understood by using a core-shell model, where the magnetic interactions are adjusted at the surface whereas those in the core are similar to those in the bulk crystal. The Monte Carlo calculation for the DyMn_2O_5 nanoparticles with classical spins indicates that the ferromagnetic components are dominant in the surface region, and the magnetization of the magnetically frustrated nanoparticle behaves as a quasi-free spin. The magnetic measurement results are qualitatively consistent with the Monte Carlo calculation results. These results indicate that the observed behaviors originate from the quasi-free spin around the surface that was induced by the frustration of the magnetic interaction. Structural analysis indicated a pronounced size dependence of the lattice constant. Particles smaller than ~ 12 nm have distorted crystallographic structures compared to those of the bulk crystal, and the tendency of distortion in the ab plane increase with decreasing particle size. The distortion of the crystallographic structures involves changes in the Mn-O-Mn bond angles, which modify the magnetic interactions. In fact, anomalous changes in the magnetic properties and crystallographic structures simultaneously occur for the particles smaller than ~ 12 nm. The present results suggest that the magnetic properties of the DyMn_2O_5 nanoparticles have a prominent correlation with the changes in the crystallographic structure. DyMn_2O_5 has complex magnetic interactions, such as the coexistence of antiferromagnetic and ferromagnetic interactions with magnetic frustration [9,15,27,28]. In particular, the interactions between Mn^{4+} ($2\mu_B$) and Mn^{3+} ($3/2\mu_B$) are sensitive to the crystallographic distortions. For example, when an electron at an e_g orbital undergoes hopping to the other e_g

orbitals in the Mn^{3+} sites, the interaction is ferromagnetic; otherwise, it is an antiferromagnetic interaction. The possibility of hopping strongly depends on the Mn-O-Mn bond angle and the orbital structures. Thus, a small distortion can alter the sign of the interactions. Since the Mn-O-Mn bond angle and the orbital structures at the surface are different from those in the bulk crystal, the interactions can be strongly modified near the surface, which leads to a release of a portion of the magnetic frustration as well as drastic changes in the Weiss temperature, coercive field, and magnetic anisotropy.

V. CONCLUSION

We synthesized DyMn_2O_5 nanoparticles of particle sizes 7 to 20 nm in the pores of SBA-15 and investigated their crystal structures and magnetic properties through TEM, XRD, and magnetic measurements and Monte Carlo calculations. The magnetic measurement results are qualitatively consistent with the Monte Carlo calculations. The experimental results indicated a correlation between the magnetic properties and the distortion of the crystallographic structures. As a result, the lattice constants of the DyMn_2O_5 nanoparticles exhibit noticeable changes below ~ 12 nm, especially in the *ab* plane, and the deviations in the lattice constants from those of the bulk crystal increase with decreasing particle size. The crystallographic structures of the nanoparticles are distorted from that of the bulk crystal, especially in the *ab* plane. This distortion is enhanced with decreasing particle size. As the particle size decreases, the blocking temperature and coercive field decrease monotonically for particles larger than ~ 12 nm, and maintain a nearly constant value for those below

12 nm. Because of the effects of the surface characteristics of nanoparticles, the Weiss temperature of the nanoparticles change from a negative to positive value as the particle size decreases to less than 12 nm. These behaviors suggested that the properties of the surface, where ferromagnetic interactions are prevailing, are dominant for particles smaller than 12 nm. Therefore, the nanoparticles exhibit the coercivity due to the ferromagnetic interactions at the surface of the nanoparticles. The experimental results suggested that some magnetic interactions at the surface become ferromagnetic and release a portion of the magnetic frustration owing to the distortion of the crystallographic structure. As a result, ferromagnetic interactions are dominant at the surface, and nanoparticles smaller than 12 nm exhibit a ferromagnetic Weiss constant.

ACKNOWLEDGMENTS

This work was supported by a Grant-in-Aid for Young Scientists (B) (No. 25870999) from the Ministry of Education, Culture, Sports, Science and Technology (MEXT) of Japan. The synchrotron radiation experiments were performed at the BL-8B beamline located in the Photon Factory (Proposals No. 2011G511 and No. 2013G523) and at the BL02B2 beamline located in the SPring-8 (Proposal No. 2011A1934). The TEM experiment was performed using the JEM-2100 at the Division of Material Science, the Advanced Research Support Center, Ehime University. The authors would like to thank Mr. Y. Ando of the Kyushu Institute of Technology, Associate Prof. C. Moriyoshi and Prof. Y. Kuroiwa of the Hiroshima University for their kind help with the experimental measurements.

-
- [1] T. Zhang, X. P. Wang, Q. F. Fang, and X. G. Li, *Appl. Phys. Rev.* **1**, 031302 (2014).
 - [2] A. Asamitsu, Y. Moritomo, Y. Tomioka, T. Arima, and Y. Tokura, *Nature (London)* **373**, 407 (1995).
 - [3] T. Kimura, T. Goto, H. Shintani, K. Ishizaka, T. Arima, and Y. Tokura, *Nature (London)* **426**, 55 (2003).
 - [4] T. Tajiri, H. Deguchi, S. Kohiki, M. Mito, S. Takagi, K. Tsuda, and Y. Murakami, *J. Phys. Soc. Jpn.* **75**, 113704 (2006).
 - [5] T. Tajiri, H. Deguchi, S. Kohiki, M. Mito, S. Takagi, M. Mitome, Y. Murakami, and A. Kohno, *J. Phys. Soc. Jpn.* **77**, 074715 (2008).
 - [6] T. Tajiri, N. Terashita, K. Hamamoto, H. Deguchi, M. Mito, Y. Morimoto, K. Konishi, and A. Kohno, *J. Magn. Magn. Mater.* **345**, 288 (2013).
 - [7] T. Tajiri, M. Harazono, H. Deguchi, M. Mito, A. Kohno, and S. Kohiki, *Jpn. J. Appl. Phys.* **49**, 06GH04 (2010).
 - [8] M. Fukunaga and Y. Noda, *J. Phys. Soc. Jpn.* **79**, 054705 (2010).
 - [9] K. Cao, G.-C. Guo, D. Vanderbilt, and L. He, *Phys. Rev. Lett.* **103**, 257201 (2009).
 - [10] L. M. Volkova and D. V. Marinin, *J. Phys.: Condens. Matter* **21**, 015903 (2009).
 - [11] H. Kimura, S. Kobayashi, Y. Fukuda, T. Osawa, Y. Kamada, Y. Noda, I. Kagomiya, and K. Kohn, *J. Phys. Soc. Jpn.* **76**, 074706 (2007).
 - [12] J. A. Alonsoy, M. T. Casaisy, M. J. Martínez-Lopey, J. L. Martínezy, and M. T. Fernández-Díaz, *J. Phys.: Condens. Matter* **9**, 8515 (1997).
 - [13] C. R. dela Cruz, F. Yen, B. Lorenz, M. M. Gospodinov, C. W. Chu, W. Ratcliff, J. W. Lynn, S. Park, and S.-W. Cheong, *Phys. Rev. B* **73**, 100406(R) (2006).
 - [14] T. C. Han and J. G. Lin, *J. Appl. Phys.* **99**, 08J508 (2006).
 - [15] G. R. Blake, L. C. Chapon, P. G. Radaelli, S. Park, N. Hur, S.-W. Cheong, and J. Rodríguez-Carvajal, *Phys. Rev. B* **71**, 214402 (2005).
 - [16] A. F. García-Flores, E. Granado, H. Martinho, R. R. Urbano, C. Rettori, E. I. Golovenchits, V. A. Sanina, S. B. Oseroff, S. Park, and S.-W. Cheong, *Phys. Rev. B* **73**, 104411 (2006).
 - [17] S. C. Abrahams and J. L. Bernstein, *J. Chem. Phys.* **46**, 3776 (1967).
 - [18] F. Kagawa, M. Mochizuki, Y. Onose, H. Murakawa, Y. Kaneko, N. Furukawa, and Y. Tokura, *Phys. Rev. Lett.* **102**, 057604 (2009).
 - [19] S. B. Wilkins, T. R. Forrest, T. A. W. Beale, S. R. Bland, H. C. Walker, D. Mannix, F. Yakhou, D. Prabhakaran, A. T. Boothroyd, J. P. Hill, P. D. Hatton, and D. F. McMorrow, *Phys. Rev. Lett.* **103**, 207602 (2009).
 - [20] M. Mochizuki and N. Furukawa, *Phys. Rev. B* **80**, 134416 (2009).

- [21] M. Mochizuki, N. Furukawa, and N. Nagaosa, *Phys. Rev. B* **84**, 144409 (2011).
- [22] W. Ratcliff, II, V. Kiryukhin, M. Kenzelmann, S.-H. Lee, R. Erwin, J. Schefer, N. Hur, S. Park, and S.-W. Cheong, *Phys. Rev. B* **72**, 060407(R) (2005).
- [23] N. Hur, S. Park, P. A. Sharma, S. Guha, and S.-W. Cheong, *Phys. Rev. Lett.* **93**, 107207 (2004).
- [24] C. Wilkinson, F. Sinclair, P. Gardner, J. B. Forsyth, and B. M. R. Wanklyn, *J. Phys. C* **14**, 1671 (1981).
- [25] R. A. Ewings, A. T. Boothroyd, D. F. McMorrow, D. Mannix, H. C. Walker, and B. M. R. Wanklyn, *Phys. Rev. B* **77**, 104415 (2008).
- [26] D. Higashiyama, S. Miyasaka, N. Kida, T. Arima, and Y. Tokura, *Phys. Rev. B* **70**, 174405 (2004).
- [27] T. Shen, K. Cao, G.-C. Guo, and L. He, *Phys. Rev. B* **78**, 134413 (2008).
- [28] G. E. Johnstone, R. A. Ewings, R. D. Johnson, C. Mazzoli, H. C. Walker, and A. T. Boothroyd, *Phys. Rev. B* **85**, 224403 (2012).
- [29] T. Tajiri, Y. Ando, H. Deguchi, M. Mito, and A. Kohno, *Physics Procedia* **75**, 1181 (2015).
- [30] D. Zhao, J. Feng, Q. Huo, N. Melosh, G. H. Fredrickson, B. F. Chemlka, and G. D. Stucky, *Science* **279**, 548 (1998).
- [31] N. J. O. Silva, V. S. Amaral, and L. D. Carlos, *J. Appl. Phys.* **100**, 054301 (2006).
- [32] W. S. Ferreira, J. Agostinho Moreira, A. Almeida, M. R. Chaves, J. P. Araújo, J. B. Oliveira, J. M. Machado Da Silva, M. A. Sá, T. M. Mendonça, P. Simeão Carvalho, J. Kreisel, J. L. Ribeiro, L. G. Vieira, P. B. Tavares, and S. Mendonça, *Phys. Rev. B* **79**, 054303 (2009).
- [33] J.-S. Zhou and J. B. Goodenough, *Phys. Rev. B* **77**, 132104 (2008).
- [34] B. H. Kim and B. I. Min, *Phys. Rev. B* **80**, 064416 (2009).
- [35] R. Kajimoto, H. Mochizuki, H. Yoshizawa, H. Shintani, T. Kimura, and Y. Tokura, *J. Phys. Soc. Jpn.* **74**, 2430 (2005).
- [36] J. Dieckhoff, D. Eberbeck, M. Schilling, and F. Ludwig, *J. Appl. Phys.* **119**, 043903 (2016).
- [37] R. H. Kodama and A. E. Berkowitz, *Phys. Rev. B* **59**, 6321 (1999).
- [38] R. H. Kodama, S. A. Makhlof, and A. E. Berkowitz, *Phys. Rev. Lett.* **79**, 1393 (1997).